IEEE Access
Multidisciplinary | Rapid Review | Open Access Journal

Received June 27, 2020, accepted July 12, 2020, date of publication July 15, 2020, date of current version July 24, 2020.

Digital Object Identifier 10.1109/ACCESS.2020.3009431

Dual-Band Dual-Polarized Scalable Antenna Subarray for Compact Millimeter-Wave 5G Base Stations

HSIN-NAN HU, FEI-PENG LAI, AND YEN-SHENG CHEN, (Member, IEEE)
Department of Electronic Engineering, National Taipei University of Technology, Taipei 10608, Taiwan

Corresponding author: Yen-Sheng Chen (yschen@ntut.edu.tw)

This work was supported by the Ministry of Science and Technology, Taiwan, under Contract MOST 109-2636-E-027-004.

ABSTRACT A dual linearly-polarized antenna subarray that operates at 28 GHz and 38 GHz is proposed for fifth generation (5G) base stations. In contrast to earlier millimeter-wave base-station antennas that implement individual single-band antennas, simultaneous realization of dual-band operation can save space and cost. In addition, the proposed subarray depicts dual polarizations, improving signal reliability through polarization diversity. Furthermore, the proposed subarray is scalable and expandable in size and aperture. The proposed antenna subarray consists of 2×2 dual off-center-fed dipoles. The dual-band feature is obtained by tailoring the structure for expanding current pathways and impedance bandwidths. Accordingly, the impedance bandwidths for the lower and higher bands are 27.2–30.2 GHz and 35.7–40.3 GHz, respectively. When uniformly-distributed currents are excited, the proposed antenna shows broadside radiation with peak gain of 13.1 dBi at 28 GHz and 13.2 dBi at 38 GHz. When various current phases are excited, the subarray provides a scanning range of $\pm 18°$. The scalability is demonstrated by an example large-scale array that comprises 4×4 elements. The *S*-parameters are robust, and the gain is enhanced as 19.6 dBi at 28 GHz and 17.8 dBi at 38 GHz. Meanwhile, a broader scanning range of $\pm 45°$ can be obtained.

INDEX TERMS 5G mobile communication, antenna arrays, base stations, multifrequency antennas.

I. INTRODUCTION

Recently, the fifth generation (5G) wireless communication technologies have been emerging into research fields. While both NR1 and NR2 have gathered great importance, the NR2 frequency bands, which utilize millimeter-wave wireless communication, provide more significant expansion of bandwidth and improve higher data rate. In particular, the Federal Communication Commission (FCC) has assigned both 28-GHz and 38-GHz bands [1], including n257 (26.50–29.50 GHz), n258 (24.25–27.50 GHz), n260 (37.00–40.00 GHz), and n261 (27.50–28.35 GHz), for 5G NR ecosystem development. However, millimeter-wave communication causes relatively high path loss and penetration loss [2]. To compensate these losses, the base stations must employ high-gain antennas and a digital beamforming scheme. Furthermore, the millimeter-wave 5G base stations are desired to have light weight and compact size, so the antenna design is required to depict high gain within a compact volume.

Earlier studies have proposed several 28/38 GHz antennas for the base stations [3]–[28]. Most of the designs aim at single bands on either 28 GHz [3]–[15] or 38 GHz [16]–[20]. Some studies propose dual-band structures that operate at both 28 GHz and 38 GHz [21]–[28]. For future millimeter-wave 5G base stations, simultaneous realization of dual-band operation can save space and cost, and thus the dual-band antenna arrays show greater potential for serving compact base stations. However, the design of dual-band arrays is challenging. The first challenge is to synthesize dual resonances on one antenna element. Even though a dual-band antenna can be generated, when multiple elements form into an array, the second challenge is bandwidth reductions and frequency detuning caused by mutual coupling between elements. Furthermore, as the physical spacing between elements is fixed, the electrical spacing in terms of the 38-GHz resonance is larger. Thus, the larger electrical spacing may cause grating lobes, which reduce the antenna gain.

The associate editor coordinating the review of this manuscript and approving it for publication was Adnan Kavak.

TABLE 1. Antenna performance for millimeter-wave 5G base stations.

No.	Frequency band (GHz)	Size (mm^2)	Number of elements	Peak gain (dBi)	Polarization	Scalability
[3]	28	20.0 × 26.0	1 × 1	7.1	Dual linear	No
[4]	28	31.0 × 31.0	1 × 1	9.2	Dual linear	No
[5]	28	8.0 × 8.0	1 × 1	7.2	Dual linear	Arbitrary size
[6]	28	4.2 × 55.3	8 × 1	16.0	Linear	Arbitrary size
[7]	28	9.8 × 71.0	12 × 1	15.7	Linear	Arbitrary size
[8]	28	N.A.	1 × 5	N.A.	Linear	Arbitrary size
[9]	28	50.0 × 50.0	6 × 6	17.5	Linear	No
[10]	28	N.A.	1 × 4	12.5	Linear	Arbitrary size
[11]	28	N.A.	7 × 1	14.7	Linear	Arbitrary size
[12]	28	30.2 × 30.2	3 × 3	15.1	Dual linear	No
[13]	28	25.0 × 25.0	5 × 3	14.8	Linear	No
[14]	28	10.7 × 10.7	2 × 2	10.4	Linear	Arbitrary size
[15]	28	10.7 × 17.8	1 × 2	7.5	Linear	Arbitrary size
[16]	38	20.0 × 20.0	2 × 2	10.8	Dual linear	No
[17]	38	N.A.	10 × 1	N.A.	Linear	Arbitrary size
[18]	38	8.8 × 9.8	2 × 2	7.7	Linear	Arbitrary size
[19]	38	N.A.	1 × 8	N.A.	Linear	Arbitrary size
[20]	38	N.A.	4 × 1	11.8	Linear	Arbitrary size
[21]	28/38	22.0 × 18.0	1 × 4	12.6/13.0	Linear	12 subarrays
[22]	28/38	13.0 × 20.0	4 × 2	12.1/13.5	Linear	12 subarrays
[23]	28/38	100. 0 × 20.0	1 × 13	11.6/12.1	Linear	No
[24]	28/38	45.0 × 180.0	4 × 1	7.8/8.4	Multi-polarized	8 subarrays
[25]	28/38	45.0 × 180.0	4 × 1	8.3/8.0	Multi-polarized	8 subarrays
[26]	28/38	26.0 × 14.0	1 × 2	1.3/1.8	Dual linear	No
[27]	28/38	26.0 × 21.0	3 × 3	12.0/9.8	Linear	No
[28]	28/38	50.8 × 12.0	1 × 4	4.8/9.4	Linear	No
This study (subarray)	28/38	34.0 × 36.0	2 × 2	13.1/13.2	Dual linear	Arbitrary size
This study (array)	28/38	66.5 × 70.0	4 × 4	19.6/17.8	Dual linear	Arbitrary size

More explicitly, the antenna performances in the literature concerning millimeter-wave 5G base stations are I summarized in Table 1. Some limitations can be observed from the earlier designs that have dual-band resonances [21]–[28]. First of all, several dual-band antenna arrays have only single polarization [21]–[23], [27], [28], but multi-polarized antenna design enables a receiver to take advantage of both the co-polarized and the cross-polarized states. Second, although some subarrays can be arranged as a large-scale antenna array, the aperture and size of the final design are fixed [21]–[28]. It is difficult to adapt these designs to base stations with arbitrary size, as a scalable or expandable feature is lacking. Third, more studies should be conducted to enhance the antenna performance in the literature. For example, the compactness of the subarray layout can be further improved [21], [22], [24], [25], and the scanning range is desired to be increased [21], [23].

The goal of this paper is to present a scalable dual-band subarray that can operate on both the 28-GHz and 38-GHz frequency bands. The distinct features of the proposed design are threefold. First of all, the proposed subarray implements dual polarizations for the dual-band operation, providing the advantage of polarization diversity that improves signal reliability. Second, the proposed subarray is scalable and expandable in size and aperture. Not only the unit element and the subarray depict desired S-parameters and radiation features, but integrated arrays with arbitrary size still provide good impedance characteristics and enhanced gain. This feature makes the proposed design provide optimum radiation performance despite the change of available antenna design

space. Third, the proposed subarray provides an enhanced scanning range, which can reduce the number of required sub-sectors. These distinguishing characteristics can overcome the limitations in the literature.

The proposed subarray consists of 2 × 2 elements, demonstrating broad bandwidths (27.2–30.2 GHz and 35.7–40.3 GHz) and high gain (13.1 dBi at 28 GHz and 13.2 dBi at 38 GHz) within a compact footprint (34.0 × 36.0 mm^2). The unit element comprises dual off-center-fed dipoles [29]. By tailoring the current paths on the structure, dual-band operation with enhanced bandwidths can be obtained. Furthermore, the topology of the subarray and the separation between elements are investigated, and the optimum structure is determined in terms of S-parameters and radiation performance. To demonstrate the scalability, the proposed subarrays are integrated as a large-scale array that consists of 2 × 2 subarrays. The resultant impedance bandwidths are 26.2–28.5 GHz and 34.5–44.7 GHz, and the peak gain at 28 GHz and 38 GHz are 19.6 dBi and17.8 dBi, respectively. In addition, the envelop correlation coefficients (ECCs) and the beam scanning range are examined, and the antenna performances are compared with the state-of-the-art.

II. UNIT ELEMENT

This section describes the design, analysis, and validation of the dual-band dual-polarized unit element. Full-wave simulation is carried out using Ansoft HFSS.

A. ANTENNA DESIGN

Figure 1 is the configuration of the proposed unit element, which consists of two layers separated by a 2.5-mm air spacer. The top and bottom layers are constructed on Rogers Duroid RT5880 (dielectric constant $\varepsilon_r = 2.2$ and loss tangent $\tan\delta = 0.0009$) with a thickness of 0.5 mm and 0.8 mm, respectively. The proposed antenna is comprised of two pairs of off-center-fed dipoles above a conducting ground plane, which locates below the bottom layer and shields the antenna from the loading effect due to other electronics. The two dipoles are placed orthogonally, fed individually to excite horizontal and vertical polarization (H-pol and V-pol), respectively, where the feeding points are denoted by F_1 and F_2. In contrast to conventional narrow-strip dipoles, which cannot provide a broadband resonance, the proposed structure applies a top hat to the ends of both arms. The top hats result in a planar dumbbell-shaped dipole [30], improving impedance bandwidths by increasing the current pathways to the top of the antenna. However, the two hats of the dipole are not realized on the same layer; instead, the two hats are constructed on separated layers. The feed line can be implemented through a 50-Ω Sub-Miniature Push-on Micro (SMPM) connector [31], which depicts advantages of compact size, reducing system weight while offering high reliability.

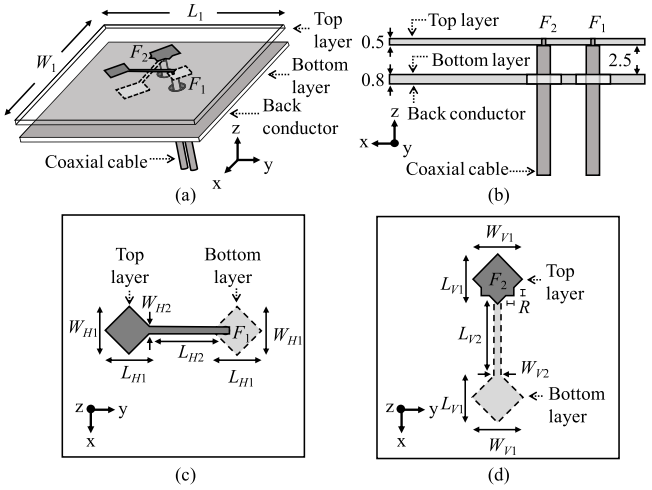

FIGURE 1. Geometry of the dual off-center-fed dipoles. (a) Three-dimensional view. (b) Side view (unit: mm). (c) H-pol and (d) V-pol configurations.

The antenna geometry is designed and optimized to generate the dual-band resonances. For the H-pol (V-pol) dipole, the geometric parameters include the length and width of the top-loaded hat, L_{H1} (L_{V1}) and W_{H1} (W_{V1}), respectively, and the length and width of the central narrow strip, L_{H2} (L_{V2}) and W_{H2} (W_{V2}), respectively. As an offset feeding scheme is adopted, the H-pol and V-pol dipoles are asymmetric. To further improve the dual-band impedance bandwidths, a pair of stair-wise patch is integrated to one of the hat of the V-pol dipole, serving the antenna as an additional impedance matching technique. The finalized geometric parameters are $L_{H1} = 5.0$ mm, $W_{H1} = 5.0$ mm, $L_{H2} = 7.0$ mm, $W_{H2} = 0.7$ mm, $L_{V1} = 6.0$ mm, $W_{V1} = 6.0$ mm, $L_{V2} = 7.0$ mm, $W_{V2} = 0.7$ mm, $R = 1.0$ mm, $L_1 = 25.0$ mm, and $W_1 = 23.0$ mm.

To explain the operating principle of the proposed antenna, both parametric effects and surface current distributions are analyzed. Considering the H-pol dipole, W_{H1} is varied over three levels: $W_{H1} = 4.0$ mm, $W_{H1} = 5.0$ mm, and $W_{H1} = 6.0$ mm, while the other parameters are fixed as the finalized value. Only the H-pol element is excited, and the resultant input reflection coefficients are exhibited in Figure 2(a). As the width increases, the resonant frequency at the lower band is shifted from 27.5 GHz to 29.2 GHz. Meanwhile, the resonant frequency at the higher band varies over 37.2–37.8 GHz. Next, L_{H1} is varied over $L_{H1} = 4.0$ mm, $L_{H1} = 5.0$ mm, and $L_{H1} = 6.0$ mm, respectively; as a result, the simulated impedance matching is shown in Figure 2(b). As the length of L_{H1} becomes longer, the resonant frequencies at the lower and higher bands are altered from 27.1 GHz to 29.2 GHz and from 34.5 GHz to 39.6 GHz, respectively. Finally, L_{H2} is modified from 6.0 mm to 8.0 mm. The resultant responses are provided in Figure 2(c). Although dual-band performance can still be observed, the resonant frequencies at the lower (higher) band are 26.9 GHz, 28.6 GHz, and 31.0 GHz (36.0 GHz, 37.1 GHz, and 38.0 GHz), respectively. These parametric studies further suggest that W_{H1}, L_{H1}, and L_{H2} have significant effects for both the 28/38 GHz resonances.

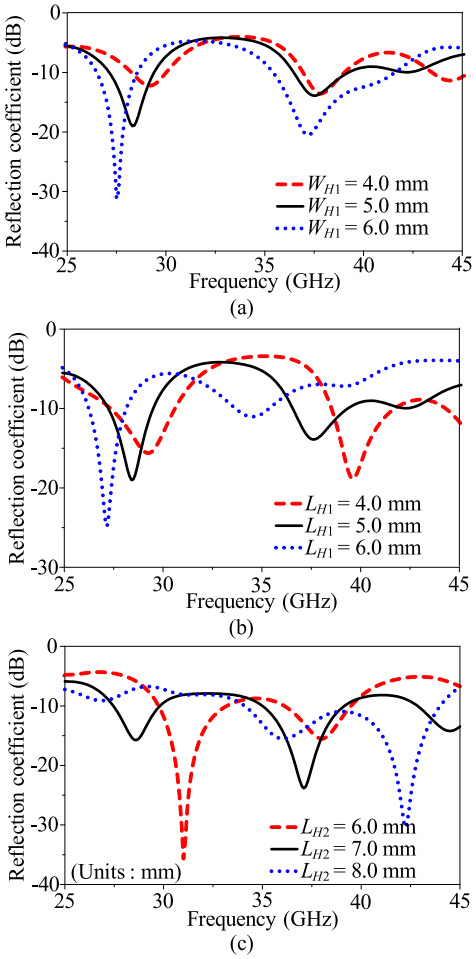

FIGURE 2. Parametric analysis of the off-center-fed dipole. Effect of the variation of (a) W_{H1}, (b) L_{H1}, and (c) L_{H2}.

To explain the mechanism of two resonances, the surface current distributions on the proposed antenna are presented in Figure 3. The overall current distributions can be evaluated as the sum of the travelling-wave currents and the standing-wave currents [32]. Considering the H-pol dipole at the resonance of 28 GHz, at $t = 0$ and $t = T/4$ (T denotes the period of oscillation at each frequency), the maximum current amplitude occurs at the offset feeding point, F_1, instead of the phase center of the dipole, which is the current maximum of a conventional center-fed dipole. On the other hand, the minimum current amplitude is at the opposite location to the feeding point, A. This indicates that the traveling-wave currents are more significant while the standing-wave currents are weak. For the resonance at 38 GHz, the currents depict the maximum at the feeding point, F, for both times. At $t = 0$, the currents show the minimum amplitude around A; however, at $t = T/4$, the currents with the maximum amplitude flow around the edge of A. This indicates that the traveling-wave and standing-wave currents are revealed alternatively. As this unit element provides two current pathways with different lengths, combining the two resonances enable

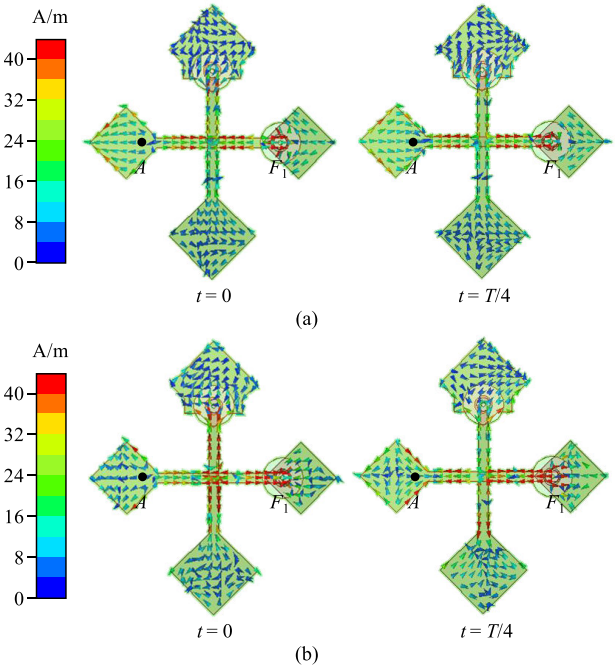

FIGURE 3. Surface current distributions of the proposed unit element. (a) 28 GHz. (b) 38 GHz.

multiband operation. Thus, the design rule of this antenna is to adjust the geometric parameters of the structure, namely, L_{H1}, L_{H2}, and W_{H1}, to control the current flowing through the upper and lower sides of the dipole.

B. PERFORMANCE

The proposed antenna structure is fabricated and tested. Figure 4 is the photograph of the test pieces for the dual-band antenna element. The impedance matching is shown in Figure 5. The simulated impedance bandwidths are 27.6–30.8 GHz and 35.4–38.9 GHz, and the measured ones are 27.8–29.9 GHz and 36.1–38.3 GHz. Dual-band impedance matching is achieved, and the simulated results agree well with the measured ones. Moreover, the isolation between the H-pol and V-pol feeding ports is presented in Figure 6. At the resonance of 28 GHz, the simulated and measured isolation are 15.4 dB and 14.3 dB, respectively. At 38 GHz, the simulated and measured isolation are 22.0 dB

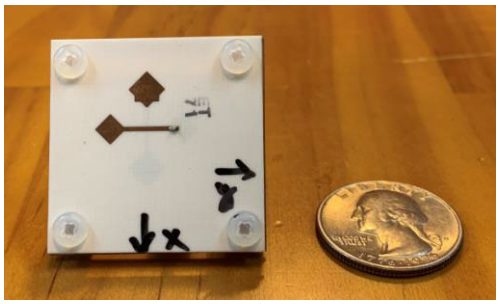

FIGURE 4. Photograph of the fabricated antenna prototype.

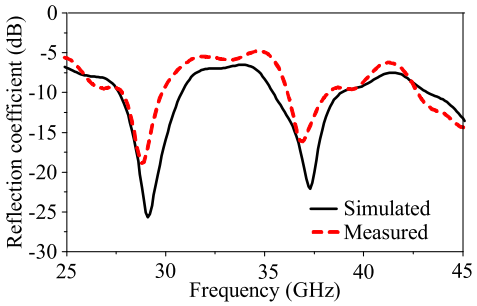

FIGURE 5. Reflection coefficients of the off-center-fed dipole.

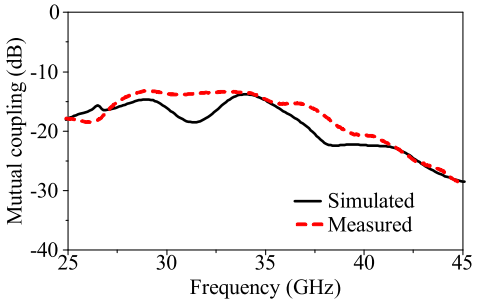

FIGURE 6. Isolation between the H-pol and V-pol dipoles.

and 17.4 dB, respectively. Although the isolation between the H-pol and V-pol ports is about 15 dB at 28 GHz, this isolation can be enhanced using signal processing algorithms at a baseband or intermediate-frequency (IF) level [33]–[36]. As multipath propagation, rainfall, equipment imperfections, and antenna misalignment degrade the isolation between the H-pol and V-pol signals, state-of-the-art MIMO communication systems must implement interference cancellation techniques for the H-pol and V-pol mutual coupling. For example, Kalman-based algorithms can jointly recover the phase of both the co-polarized signal and the interfering one using carrier phase synchronization [33], [34]. An algorithm based on soft constraint satisfaction (SCS) is proposed to eliminate mutual coupling between the H-pol and V-pol signals using a digital signal filter at the baseband [35]. A joint equalizer is proposed to deal with the mutual coupling between H-pol and V-pol ports and inter-symbol interference (ISI) simultaneously based on Least Mean Square (LMS) [36]. These techniques can create more significant improvements of isolation as compared to Radiofrequency (RF) implementation alone.

The radiation characteristics of the unit element are also measured. Figure 7 exhibits the realized gain patterns. At the resonance of 28 GHz, the simulated and measured broadside gain are 6.9 dBi and 5.7 dBi, respectively. On the x-z plane, the simulated and measured broadside cross-polarization discriminations (XPDs) are 25.1 dB and 24.2 dB, respectively. On the y-z plane, the simulated and measured results become 23.4 dB and 24.1 dB, respectively. At 38 GHz, the simulated and measured broadside gain are 5.3 dBi and 5.5 dBi, respectively. The simulated and measured broadside XPDs on the x-z plane are 22.9 dB and 20.0 dB, respectively. On the y-z plane, the simulated and measured results become 21.6 dB and 22.8 dB, respectively. Thanks to the back conductor, the unit antenna element depicts broadside radiation

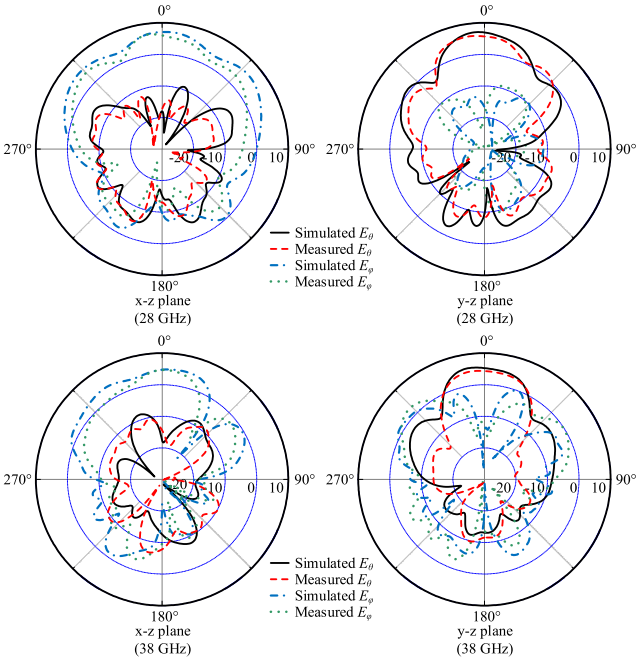

FIGURE 7. Realized gain patterns of the off-center-fed dipole at 28 GHz and 38 GHz (unit: dBi).

at both the resonant frequencies. Figure 8 provides the simulated and measured antenna efficiency, which include radiation efficiency as well as impedance matching. The simulated (measured) efficiency at 28 GHz and 38 GHz are 86.5% (88.8%) and 85.4% (69.7%), respectively. Within the operating impedance bandwidth, the measured efficiency is generally larger than 50%, which is sufficient for a millimeter-wave application. Finally, the simulated and measured realized peak gain are provided in Figure 9. The simulated and measured realized peak gain at 28 GHz are 7.4 dBi and 7.8 dBi, respectively, whereas the simulated and measured results at 38 GHz are 7.7 dBi and 5.5 dBi, respectively. These impedance and radiation characteristics validate the proposed dual-band dual-polarized antenna element.

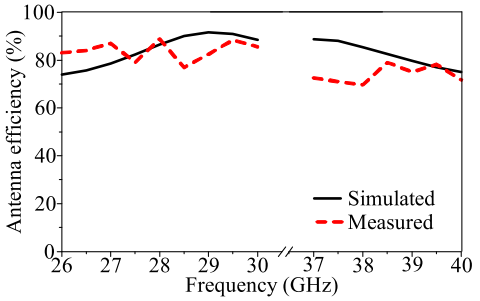

FIGURE 8. Antenna efficiency of the off-center-fed dipole.

III. ANTENNA SUBARRAY

A. ANTENNA DESIGN

This section describes a scalable subarray that consists of 2 × 2 identical unit elements. Figure 10 presents the

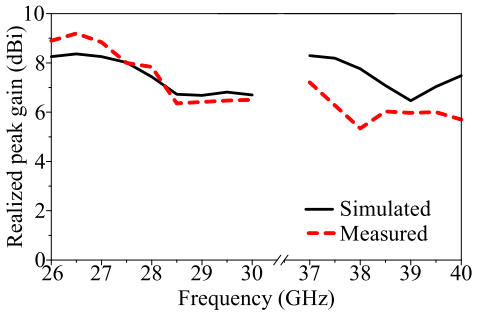

FIGURE 9. Realized peak gain of the off-center-fed dipole.

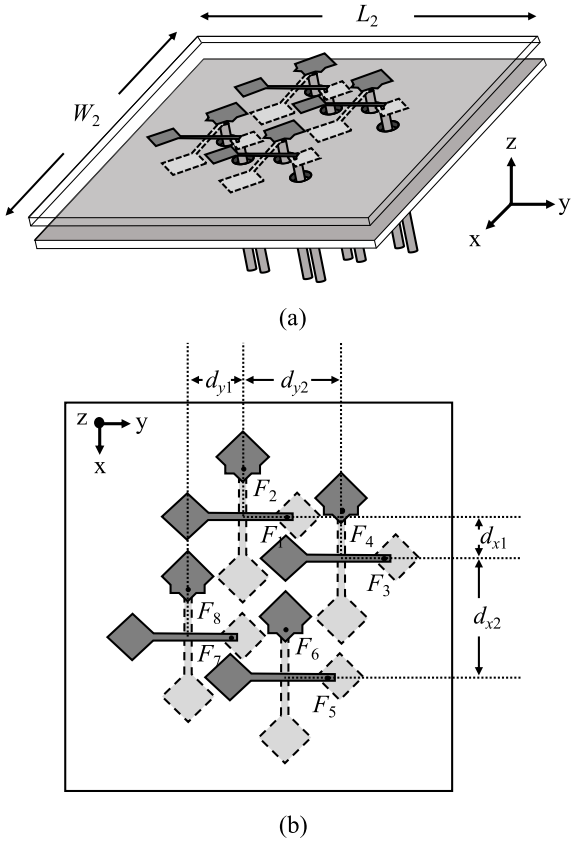

FIGURE 10. Geometry of the proposed antenna subarray. (a) Three-dimensional view. (b) Top view.

geometry of the proposed subarray. This planar subarray is arranged in a quasi-triangular lattice. That is, both row and column are shifted from the original square lattice position. This arrangement narrows the separation between elements in both the x and y directions. The separations are arranged as $d_{x1} = 4.0$ mm, $d_{x2} = 13.0$ mm, $d_{y1} = 6.0$ mm, and $d_{y2} = 10.5$ mm, where d_{x1}, d_{x2}, d_{y1}, and d_{y2} are the distance between the phase centers of adjacent elements. For a dual-band antenna arrays at 28/38 GHz, the electrical separation between the 38-GHz resonances is naturally larger. This increases the potential risk from grating lobes; thus, a layout with a compact separation is important for this scenario. The proposed quasi-triangular lattice can delay the existence of grating lobes and miniaturize the overall dimensions.

The proposed subarray implements 8 ports, where ports 1, 3, 5, and 7 excite H-pol radiation and ports 2, 4, 6, and 8 excite V-pol plane wave. The currents that feed these ports can be controlled by a digital beamforming module. Although the dimensions of the circuit board are $L_2 = 80$ mm and $W_2 = 80$ mm, the subarray takes up space with dimensions of only 34×36 mm^2.

To investigate the operating principle, Figure 11 presents the simulated surface current distributions of the proposed antenna subarray, where the H-pol ports are excited in phase. The current distributions of the element in the subarray are similar to the case of the unit element. For the resonance at 28 GHz, the maximum and minimum of current amplitude are the offset feeding point and the opposite location of the feed, respectively, which correspond to the resonance principle of the off-center-fed dipole. For the resonance at 38 GHz, the traveling-wave and standing-wave currents are appeared alternatively. In addition, the four elements depict similar current distributions. Accordingly, when the four elements are excited in phase, these current distributions are expected to create broadside radiation at both the frequencies.

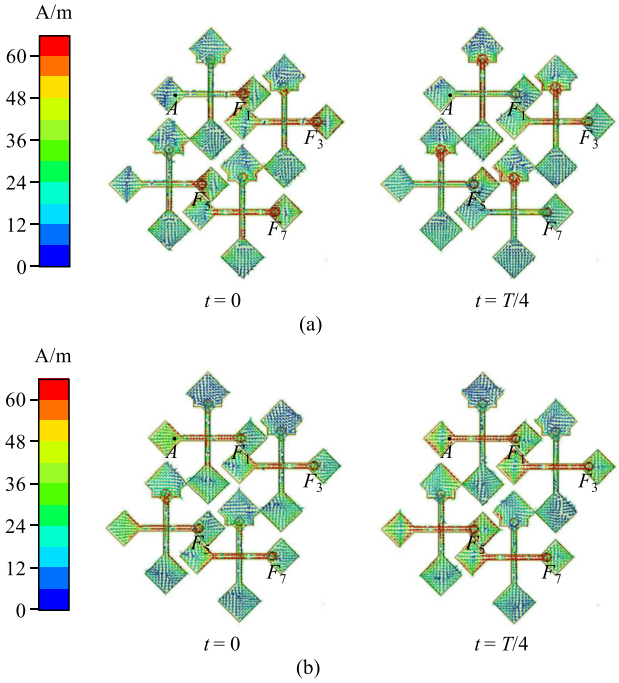

FIGURE 11. Surface current distributions of the proposed antenna subarray. (a) 28 GHz. (b) 38 GHz.

Major challenges to dual-band scalable subarrays are the avoidance of grating lobes and robust S-parameters. To demonstrate that the proposed subarray geometry can elude grating lobes, two reference configurations in a standard triangular lattice are analyzed. The geometry of the two reference designs is shown in Figure 12. Conventionally, an array in a rectangular lattice leads to a larger separation

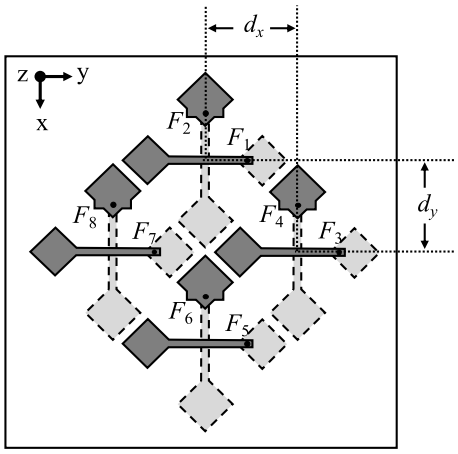

FIGURE 12. Geometry of the reference subarray design in a standard triangular lattice.

between elements; in contrast, the arrangement in a triangular lattice can make use of the design space more efficiently [37]. For the two reference subarrays, denoted by Ref1 and Ref2, the separations between the elements are $d_x = d_y = 10.0$ mm and $d_x = d_y = 9.0$ mm, respectively, where d_x and d_y are the distance between the phase centers of adjacent elements. Ref2 employs a closer separation, which leads to a more compact design and was expected to elude the occurrence of grating lobes.

First of all, the impedance matching of Ref1, Ref2, and the proposed subarray are presented in Figure 13. These results are evaluated by exciting port 1, while the other ports are terminated to match load. Both the dual bands can achieve robust matching using the three array arrangements.

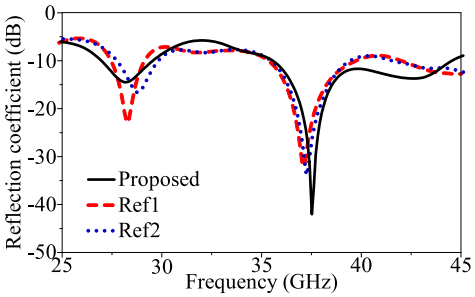

FIGURE 13. Reflection coefficients of port 1 for the three subarrays.

However, as the radiation patterns at 38 GHz are tested, Ref1 and Ref2 exhibit significant grating lobes. The four H-pol ports of the three subarrays are excited, and the resultant y-z plane patterns at 38 GHz are shown in Figure 14. Although the three subarrays provide a local maximum at the broadside direction, grating lobes occur at about ±50°. Concerning Ref1, peak gain of 10.7 dBi appears at –63°, whereas the broadside gain is 4.5 dBi. Concerning Ref2, peak gain of 8.3 dBi appears at −41°, whereas the broadside gain is 5.9 dBi. These results indicate that the reference subarray

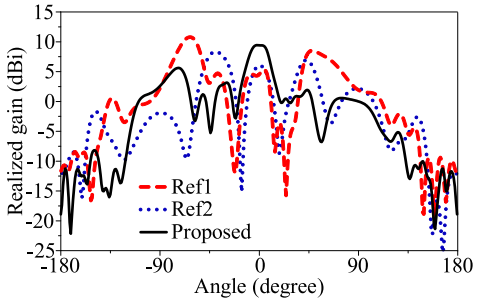

FIGURE 14. Radiation patterns of the three subarrays at 38 GHz.

geometry fails to prevent the occurrence of grating lobes. In contrast, the proposed subarray preserves the main beam to be directed broadside. The first side lobe level is 2.1 dBi, at −73°, which is lower than the broadside gain of 9.5 dBi. As a result, the proposed subarray in the quasi-triangular lattice overcomes the challenge of dual-band array design.

B. PERFORMANCE

The *S*-parameters of the subarray are tested and compared with the results of the unit element. The photograph of the test piece is presented in Figure 15. The simulated and measured impedance matching of port 1 are shown in Figure 16(a). The simulated impedance bandwidths are 27.2–30.2 GHz and 35.7–40.3 GHz, and the measured ones are 27.1–29.5 GHz and 36.1–38.3 GHz. The measured impedance bandwidths are slightly narrower than the simulated ones, but the dual-band feature is achieved. In addition, the simulated impedance matching at ports 1, 3, 5, and 7 are exhibited in Figure 16(b). The four results are highly comparable, demonstrating sufficient impedance matching at these ports. Please note that the simulated result of port 1 in Figure 16(a) is slightly different from those in Figure 16(b). In Figure 16(a), ports 2–7 are terminated to open load; on the other hand, in Figure 16(b), the other ports are terminated to match load.

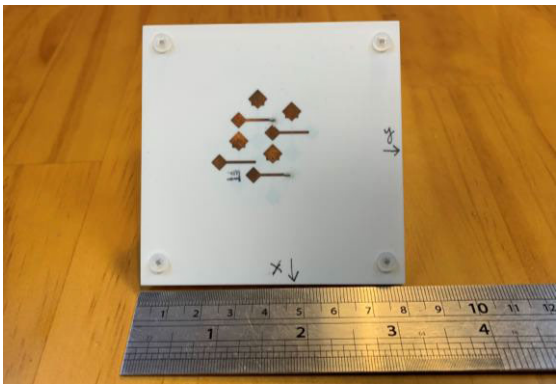

FIGURE 15. Photograph of the fabricated subarray prototype.

The simulated and measured isolation are shown in Figure 17(a). For the isolation between ports 1 and 2, the

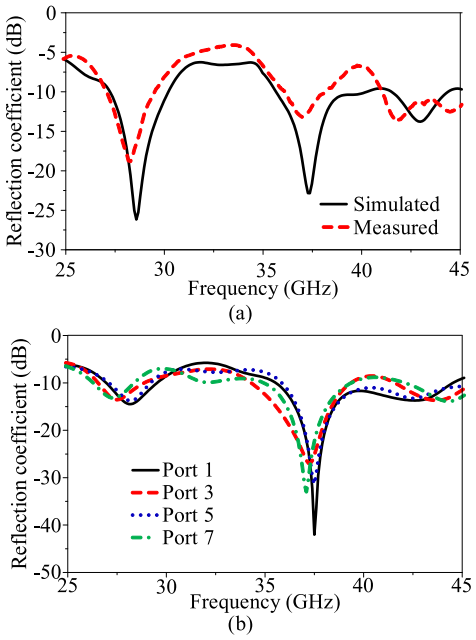

FIGURE 16. Reflection coefficients of elements in the proposed subarray. (a) Simulated and measured results of port 1. (b) Comparison of simulated results for ports 1, 3, 5, and 7.

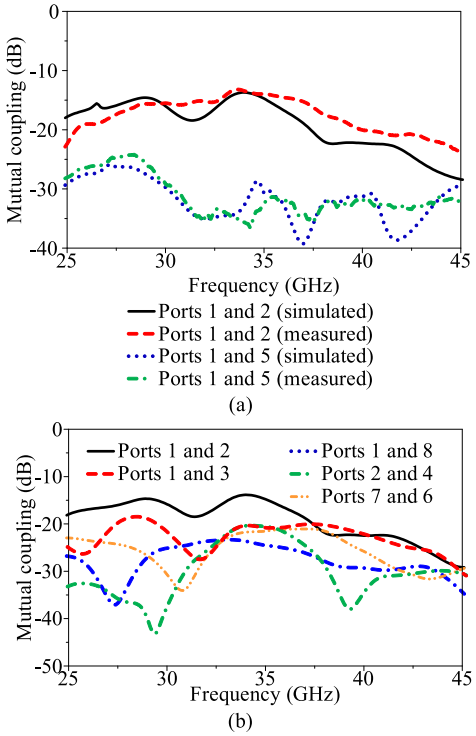

FIGURE 17. Isolation between elements in the proposed subarray. (a) Comparison of simulated and measured results. (b) Comparison of simulated results for adjacent ports.

simulated and measured isolation at 28 GHz (38 GHz) are 15.4 dB (22.0 dB) and 16.8 dB (17.4 dB), respectively. The isolation between ports 1 and 5 also depicts good agreement.

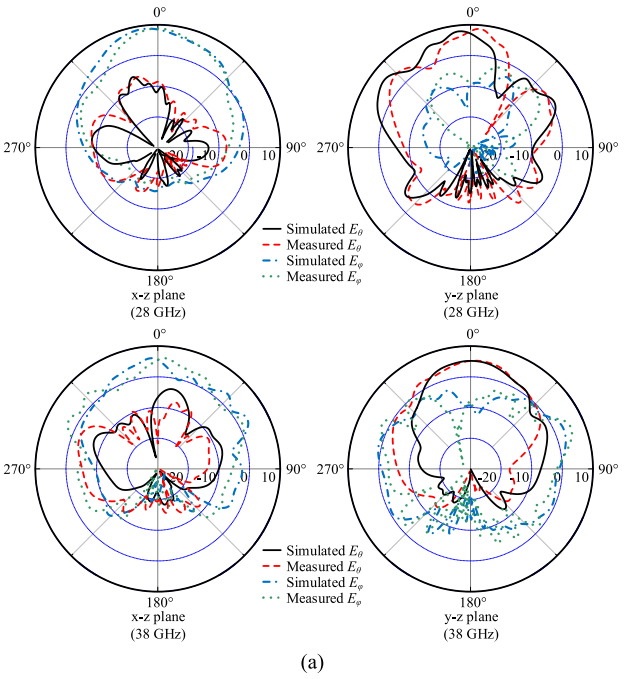

FIGURE 18. Realized gain patterns of the proposed subarray at 28 GHz and 38 GHz (unit: dBi). (a) Simulated and measured results for port 1 excited. (b) Simulated results for four ports excited simultaneously.

Additionally, the comparison of isolation for various ports is presented in Figure 17(b). The lowest isolation is the one between ports 1 and 2. Otherwise, the in-band isolation is generally greater than 20 dB.

Figure 18(a) presents the simulated and measured realized gain patterns when port 1 is excited and the other ports are terminated to open load. These results examine the agreement between simulated and measured far-field radiation characteristics. At 28 GHz, the simulated and measured broadside

XPDs on the x-z plane are 21.1 dB and 18.3 dB, respectively. On the y-z plane, the simulated and measured broadside XPDs are 17.4 dB and 18.1 dB, respectively. At 38 GHz, the simulated and measured broadside XPDs on the x-z plane are 14.4 dB and 26.9 dB, respectively. On the y-z plane, the simulated and measured broadside XPDs are 16.0 dB and 16.1 dB, respectively. The trends of the two approaches are comparable. Figure 18(b) shows the simulated gain patterns when all the H-pol or V-pol ports are excited by uniformly-distributed currents. At the resonance of 28 GHz, the H-pol and V-pol peak gain are 13.2 dBi and 9.5 dBi, respectively. At 38 GHz, the H-pol and V-pol peak gain are 10.5 dBi and 13.2 dBi, respectively. These results suggest a high-gain feature. It is noted that the proposed subarray is not tested with extra feeding networks, for digital beamforming will be employed to excite the array in future 5G base stations; thus, the measured radiation performance neglect the loss of the feeding network.

Another important performance index for 5G base stations is the envelop correlation coefficient (ECC) between ports i and j, denoted by ρ_{ij}. The ECC can be expressed in terms of the S-parameters [38]:

$$\rho_{ij} = \frac{\left|S_{ii}^{*}S_{ij} + S_{ji}^{*}S_{jj}\right|^{2}}{\left(1 - |S_{ii}|^{2} - |S_{ij}|^{2}\right)\left(1 - |S_{ji}|^{2} - |S_{jj}|^{2}\right)} \quad (1)$$

where $(i, j) \in \{(i,j)\,|1 \leq i < j \leq 8, i,j \in \mathbb{N}\}$. This expression provides predictions in several experimental environments, especially indoor environments with rich multipath propagation, which are the aim of the 5G base stations. The ECCs of the proposed antenna subarray calculated by the simulated S-parameters are shown in Figure 19(a). To confirm the validity of the results, the ECCs are also evaluated using the radiation patterns:

$$\rho_{ij} = \frac{\left|\iint_{4\pi}\left[F_i(\theta,\varphi)\cdot F_j(\theta,\varphi)\right]d\Omega\right|}{\sqrt{\iint_{4\pi}|F_i(\theta,\varphi)|^{2}\,d\Omega}\sqrt{\iint_{4\pi}\left|F_j(\theta,\varphi)\right|^{2}d\Omega}} \quad (2)$$

where $\cdot$ denotes a Hermitian inner product and $F_i(\theta, \varphi)$ is the field pattern of the antenna array when only the port i is excited and all other ports are terminated to match load. Figure 19(b) presents the calculated results, which agree well with the ECCs computed using the S-parameters. The ECCs of the proposed subarray are less than 0.03 for the dual bands, meeting the requirement of base stations that use multiple antennas.

Finally, the scanning range of this subarray is tested. The four elements are fed by currents with progressive phases, which can shift the direction of main beam. The resultant gain, pattern, and pointing angle of the main beam are recorded. In general, the highest gain occurs when the pointing angle is broadside. The wider the pointing angle, the smaller the gain is; accordingly, the difference between the gain and the maximum achievable gain is defined as scan loss. The scanning range is further defined as the range of angles that lead to 3-dB scan loss. By testing potential

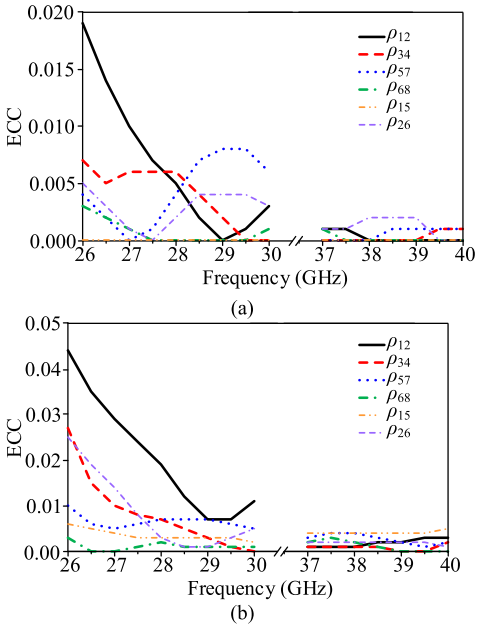

FIGURE 19. Envelop correlation coefficients of the proposed subarray computed using (a) S-parameters and (b) radiation patterns.

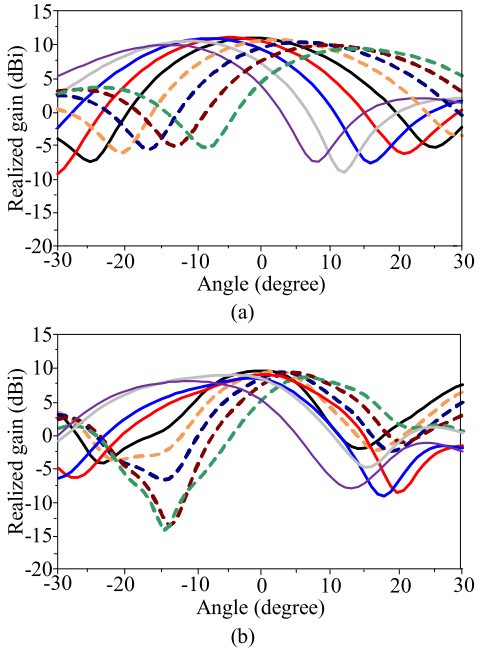

FIGURE 20. Beam scanning performance of the proposed subarray. (a) 28 GHz. (b) 38 GHz.

combinations of the progressive phases, the beam scanning performance for the subarray is depicted in Figure 20. The scanning ranges at 28 GHz and 38 GHz are ±18°. Such beam scanning performance and the isolation between ports are influenced by the separation between unit elements. Our design strategy is to select a separation that prevents grating lobes. The isolation can be enhanced using baseband and IF interference cancellation techniques, whereas the HPBW and

the beam scanning range can be improved using a larger-scale antenna array.

IV. SCALABILITY

As compared to the earlier studies regarding millimeter-wave 5G base-station antennas [21]–[28], a distinct feature of the proposed subarray is scalability in aperture and size. This section demonstrates the scalability by an example that consists of 2 × 2 identical subarrays.

Figure 21 is the geometry of the large-scale antenna array. This antenna array consists of 16 unit elements, which result in 32 ports. The separations between unit elements are identical as those described in Figure 11. Ports with odd numbers excite H-pol radiation, whereas even numbers ports excite V-pol plane wave. The dimensions of the large-scale antenna array are 66.5 × 70.0 mm^2.

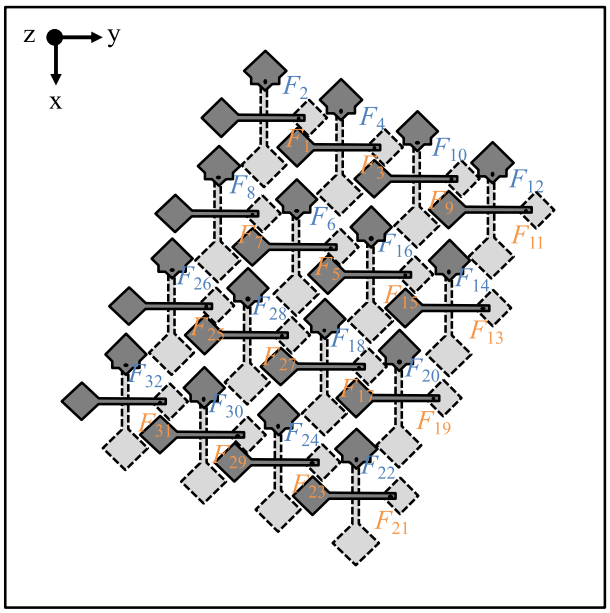

FIGURE 21. Geometry of the large-scale antenna array that consists of 2 × 2 subarrays.

The robustness of *S*-parameters and radiation features are tested. Figure 22 presents the comparison of simulated reflection coefficients for the unit element, the port 1 of the subarray, and the various ports of the large-scale array. The results are almost identical, and both the dual bands indicate good and robust impedance matching.

Figure 23 shows the realized gain patterns when all the 16 H-pol elements are excited with uniformly-distributed currents. The main beam of the antenna array is directed broadside. The peak gain at 28 GHz and 38 GHz are 19.6 dBi and 17.8 dBi, respectively. In particular, at 28 GHz, the half-power beam widths (HPBWs) on the x-z and y-z planes are 12° and 11°, respectively. At 38 GHz, the HPBWs on the x-z and y-z planes are 10° and 11°, respectively. These results indicate that the radiation performance can be enhanced by straightforwardly integrating the proposed

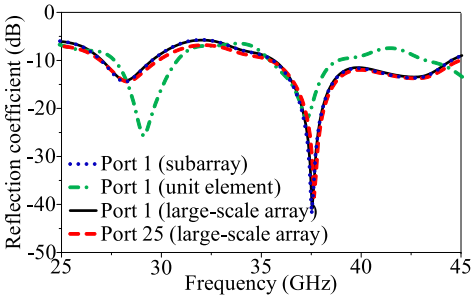

FIGURE 22. Reflection coefficients of elements in the large-scale antenna array.

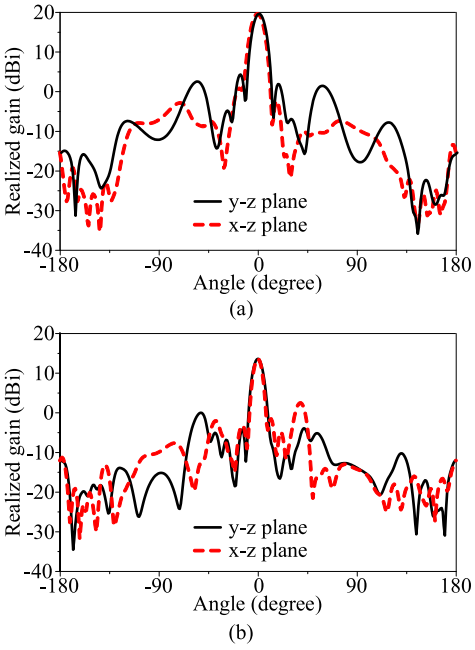

FIGURE 23. Radiation patterns of the large-scale antenna array. (a) 28 GHz. (b) 38 GHz.

subarrays. As the FCC regulation allows 28-GHz base stations to transmit at maximum effective isotropic radiated power (EIRP) of 73 dBm per polarization [39], [40], the maximum power handling of the large-scale antenna array is 53 dBm. When the proposed subarray is expanded into even larger scales, this maximum power is varied over the number of elements as well as the overall antenna gain, subject to the peak EIRP regulation. In addition, the sidelobe level (SLL) at 38 GHz is about –14 dB, which is a typical value for uniformly-excited current distributions. This SLL can be improved using two schemes. First, the SLL inversely varies as the number of elements, so an even larger-scale array will not depict a SLL as high as that for this array. Second, in general, the excitation scheme of a beamforming integrated circuit (IC) does not implement uniform distributions; in contrast, Dolph-Tchebyscheff excitations can improve the SLL based on an acceptable threshold.

Figure 24 presents the scanning range of the large-scale antenna array. The progressive phase of the feeding current is controlled so that the main beam can be pointed at various angles. The scanning ranges at 28 GHz and 38 GHz are about ±45°. By arranging the array on the surface of an octagonal prism structure, the azimuth plane can be served without communication deadzones. These characteristics validate the scalability of the proposed subarray. Although the design space of 5G base-station antennas varies over different models, the proposed subarray can exploit an available area and provide enhanced radiation performance.

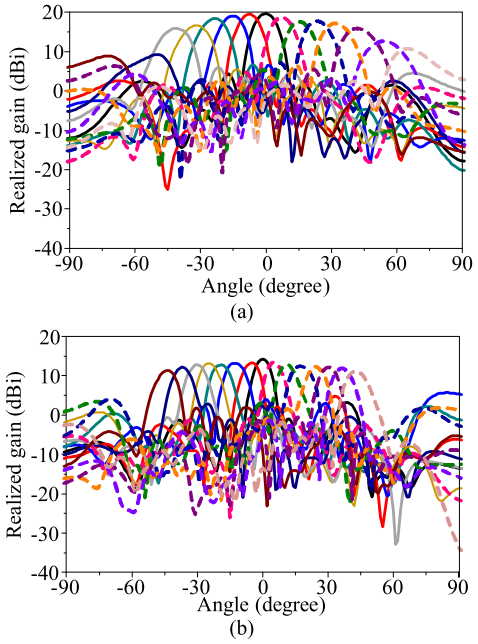

FIGURE 24. Beam scanning performance of the large-scale array. (a) 28 GHz. (b) 38 GHz.

After validating the performance of the large-scale antenna array, the proposed antenna can serve MIMO antenna systems as a 5G beam-forming unit. A scenario of the deployment of the proposed antenna is shown in Figure 25. An input signal is assigned and transmitted to a 16-way power divider. The output of the power divider is cascaded with a beamforming IC which consists of four H-pol and four V-pol channel radiofrequency (RF) control. Each channel comprises RF components including circulator, variable attenuator, variable phase shifter, high power amplifier (HPA), driver, limiter, and low noise amplifier (LNA), providing the ability to steer a radiation pattern. The four H-pol and V-pol channels are connected to the odd numbers and even numbers of ports of the proposed subarray, respectively. The kernel that controls the feed conditions for the antenna is the variable attenuator, which provides 32 dB attenuation range with 0.5 dB per step, and the variable phase shifter, which offers 360° phase shift coverage with 5.625° per step. By assigning the bit combination for the attenuator and the phase shifter, beamforming can be performed based on the signal processing

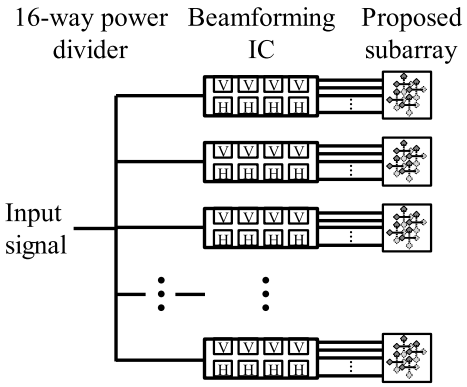

FIGURE 25. Deployment of the proposed antenna subarray in MIMO antenna systems.

results. The output port of the beamforming IC is terminated with a K-type connector. For this scenario that employs 16 beamforming ICs, the 16 RF signals are combined and controlled through the 16-way power divider. Such power dividers can be implemented using multiple stages of 2-way Wilkinson power divider structures [41], [42], which use two output ports extended and coupled through a coupled line section. Furthermore, as the proposed antenna subarray is scalable, the overall array size can be expanded. Additional antenna ports are readily connected to the channels of other beamforming ICs, so the proposed scheme can serve the MIMO antenna system that consists of 64 H-pol and 64 V-pol channels.

V. CONCLUSION

In this paper, a dual-band dual-polarized antenna subarray with scalability in aperture and size for 5G compact base stations is presented. The unit element is designed as the dual off-center-fed dipoles, which operate in 27.6–30.8 GHz and 35.4–38.9 GHz with broadside gain of 6.9 dBi at 28 GHz and 5.3 dBi at 38 GHz. By combining 2 × 2 unit elements as the subarray, the proposed antenna exhibits three distinct features. First of all, the proposed subarray provides 4 horizontal and 4 vertical feeding ports with low ECC ($\rho_{ij} < 0.03$). This mechanism can enhance transmission and reception efficiency using polarization diversity. Second, although the design space is limited to 34.0 × 36.0 mm^2, the proposed subarray provides high gain (13.1 dBi at 28 GHz and 13.2 dBi at 38 GHz), broad bandwidths (27.2–30.2 GHz and 35.7–40.3 GHz), broadside radiation, and low ECC under uniformly-distributed currents. Third, the proposed subarray can be expanded into large-scale arrays with arbitrary size. This paper demonstrates the scalability through a 4 × 4 antenna array that comprises identical unit elements. Robust S-parameters and enhanced radiation features are identified. The peak gain becomes 19.6 dBi at 28 GHz and 17.8 dBi at 38 GHz, and the scanning ranges of the dual bands are ±45°. These results validate the proposed subarray for compact millimeter-wave 5G base stations.

REFERENCES

[1] *Use of Spectrum Bands Above 24 GHz for Mobile Radio Services*, document GN Docket 14-177, Notice Proposed Rulemaking, FCC Record 89A1, Jul. 2016.

[2] T. S. Rappaport, S. Sun, R. Mayzus, H. Zhao, Y. Azar, K. Wang, G. N. Wong, J. K. Schulz, M. Samimi, and F. Gutierrez, "Millimeter wave mobile communications for 5G cellular: It will work!" *IEEE Access*, vol. 1, pp. 335–349, 2013.

[3] L. Wei, H. Hui, and W. Bin, "Dual polarization millimeter-wave antenna for microcell base station," in *Proc. IEEE Electr. Design Adv. Packag. Syst. Symp. (EDAPS)*, Haining, China, Dec. 2017, pp. 1–3.

[4] K. Gulur Sadananda, M. P. Abegaonkar, and S. K. Koul, "Gain equalized shared-aperture antenna using dual-polarized ZIM for mmWave 5G base stations," *IEEE Antennas Wireless Propag. Lett.*, vol. 18, no. 6, pp. 1100–1104, Jun. 2019.

[5] I. Hwang, H. Jo, B. K. Ahn, J. Oh, and J. Yu, "Cavity-backed stacked patch array antenna with dual polarization for mmWave 5G base stations," in *Proc. 13th Eur. Conf. Antennas Propag. (EuCAP)*, Krakow, Poland, Apr. 2019, pp. 1–5.

[6] M. K. Ishfaq, T. A. Rahman, Y. Yamada, and K. Sakakibara, "8×8 phased series fed patch antenna array at 28 GHz for 5G mobile base station antennas," in *Proc. IEEE-APS Topical Conf. Antennas Propag. Wireless Commun. (APWC)*, Verona, Italy, Sep. 2017, pp. 160–162.

[7] J. Puskely, Y. Aslan, A. Roederer, and A. Yarovoy, "SIW based antenna array with power equalization in elevation plane for 5G base stations," in *Proc. 12th Eur. Conf. Antennas Propag. (EuCAP)*, London, U.K., Apr. 2018, pp. 1–5.

[8] H. A. Diawuo and Y.-B. Jung, "Broadband proximity-coupled microstrip planar antenna array for 5G cellular applications," *IEEE Antennas Wireless Propag. Lett.*, vol. 17, no. 7, pp. 1286–1290, Jul. 2018.

[9] F.-P. Lai, H.-J. Li, C.-M. Li, P.-J. Wang, and Y.-S. Chen, "A multipart 5G base-station antenna using series-fed patch antenna sub-arrays," in *Proc. IEEE Int. Symp. Antennas Propag. USNC/URSI Nat. Radio Sci. Meeting*, Boston, MA, USA, Jul. 2018, pp. 641–642.

[10] C.-X. Mao, S. Gao, and Y. Wang, "Broadband high-gain beam-scanning antenna array for millimeter-wave applications," *IEEE Trans. Antennas Propag.*, vol. 65, no. 9, pp. 4864–4868, Sep. 2017.

[11] P. A. Dzagbletey and Y.-B. Jung, "Stacked microstrip linear array for millimeter-wave 5G baseband communication," *IEEE Antennas Wireless Propag. Lett.*, vol. 17, no. 5, pp. 780–783, May 2018.

[12] S. I. Orakwue, R. Ngah, and T. A. Rahman, "A two dimensional beam scanning array antenna for 5G wireless communications," in *Proc. IEEE Wireless Commun. Netw. Conf.*, Doha, Qatar, Apr. 2016, pp. 1–4.

[13] W. Y. Yong and A. A. Glazunov, "High gain, wideband grid array antenna for 28 GHz 5G base station," in *Proc. 13th Eur. Conf. Antennas Propag. (EuCAP)*, Krakow, Poland, Apr. 2019, pp. 1–5.

[14] M. Sonkki, S. Myllymäki, N. Tervo, M. E. Leinonen, M. Sobocinski, G. Destino, and A. Pärssinen, "Linearly polarized 64-element antenna array for mm-wave mobile backhaul application," in *Proc. 12th Eur. Conf. Antennas Propag. (EuCAP)*, London, U.K., 2018, pp. 1–5.

[15] M. S. F. Reyhan, Y. Rahayu, and F. Muhammadsyah, "The design of broadband 8 × 2 phased array 5G antenna MIMO 28 GHz for base station," *Int. J. Electr., Electron. Commun. Sci.*, vol. 12, no. 11, pp. 840–843, Oct. 2018.

[16] H. Chu and Y.-X. Guo, "A filtering dual-polarized antenna subarray targeting for base stations in millimeter-wave 5G wireless communications," *IEEE Trans. Compon., Packag., Manuf. Technol.*, vol. 7, no. 6, pp. 964–973, Jun. 2017.

[17] Y. Cao, K.-S. Chin, W. Che, W. Yang, and E. S. Li, "A compact 38 GHz multibeam antenna array with multifolded butler matrix for 5G applications," *IEEE Antennas Wireless Propag. Lett.*, vol. 16, pp. 2996–2999, 2017.

[18] Y. Rahayu, I. P. Sari, D. I. Ramadhan, and R. Ngah, "High gain 5G MIMO antenna for mobile base station," *Int. J. Electr. Comput. Eng.*, vol. 9, no. 1, pp. 468–476, Feb. 2019.

[19] C.-N. Hu, D.-C. Chang, C.-H. Yu, T.-W. Hsaio, and D.-P. Lin, "Millimeter-wave microstrip antenna array design and an adaptive algorithm for future 5G wireless communication systems," *Int. J. Antennas Propag.*, vol. 2016, pp. 1–10, Jan. 2016.

[20] L.-H. Yen, Y.-C. Huang, S.-H. Su, C.-Y. Fan, F.-H. Chu, F.-Y. Kuo, H.-C. Lu, S.-G. Mao, K.-Y. Lin, T.-C. Yen, and T.-L. Wu, "Modularized prototype of 5G mmWave base station system at 38 GHz," in *Proc. IEEE Int. Symp. Electromagn. Compat. IEEE Asia–Pacific Symp. Electromagn. Compat. (EMC/APEMC)*, Singapore, May 2018, pp. 396–398.

[21] T. Elhabbash and T. Skaik, "Design of dual-band dual-polarized MIMO antenna for mm-wave 5G base stations with octagonal prism structure," in *Proc. IEEE 7th Palestinian Int. Conf. Electr. Comput. Eng. (PICECE)*, Gaza, Palestine, Mar. 2019, pp. 1–6.

[22] M. M. M. Ali and A.-R. Sebak, "Design of compact millimeter wave massive MIMO dual-band (28/38 GHz) antenna array for future 5G communication systems," in *Proc. 17th Int. Symp. Antenna Technol. Appl. Electromagn. (ANTEM)*, Montreal, QC, Canada, Jul. 2016, pp. 1–2.

[23] R. Y. Mianroodi, H. Aliakbarian, and G. A. E. Vandenbosch, "Dual-port dual-band (28/38 GHz) SIW leaky wave antenna for 5G base stations," in *Proc. 12th Eur. Conf. Antennas Propag. (EuCAP)*, London, U.K., Apr. 2018, pp. 1–4.

[24] K. R. Mahmoud and A. M. Montaser, "Performance of tri-band multi-polarized array antenna for 5G mobile base station adopting polarization and directivity control," *IEEE Access*, vol. 6, pp. 8682–8694, Mar. 2018.

[25] K. R. Mahmoud and A. M. Montaser, "Synthesis of multi-polarised upside conical frustum array antenna for 5G mm-wave base station at 28/38 GHz," *IET Microw., Antennas Propag.*, vol. 12, no. 9, pp. 1559–1569, Jul. 2018.

[26] M. N. Hasan, S. Bashir, and S. Chu, "Dual band omnidirectional millimeter wave antenna for 5G communications," *J. Electromagn. Waves Appl.*, vol. 33, no. 12, pp. 1581–1590, Aug. 2019.

[27] S. F. Jilani and A. Alomainy, "A multiband millimeter-wave 2-D array based on enhanced Franklin antenna for 5G wireless systems," *IEEE Antennas Wireless Propag. Lett.*, vol. 16, pp. 2983–2986, 2017.

[28] S. F. Jilani and A. Alomainy, "Millimetre-wave T-shaped MIMO antenna with defected ground structures for 5G cellular networks," *IET Microw., Antennas Propag.*, vol. 12, no. 5, pp. 672–677, Apr. 2018.

[29] M. Sumi and J.-I. Takada, "Multiband antennas comprising off-center-fed dipoles for M2M applications," in *Proc. IEEE Conf. Antenna Meas. Appl. (CAMA)*, Vasteras, Sweden, Sep. 2018, pp. 1–2.

[30] Z.-Y. Zhang, X.-D. Yang, G. Fu, and S.-L. Zuo, "Wideband omnidirectional printed dipole antenna with dumbbell-shaped open sleeve for wireless communication applications," *IET Microw., Antennas Propag.*, vol. 8, no. 15, pp. 1299–1304, Dec. 2014.

[31] R. F. Amphenol, "SMP and SMPM subminiature and microminiature connectors for applications to 65 GHz," *Microw. J.*, vol. 47, pp. 32–35, Mar. 2004.

[32] J. Belrose and P. Bouliane, "The off-center-fed dipole revisited: A broadband, multiband antenna," *QST Mag.*, vol. 74, no. 8, pp. 28–34, 1990.

[33] A. Vizziello, P. Savazzi, and R. Borra, "Joint phase recovery for XPIC system exploiting adaptive Kalman filtering," *IEEE Commun. Lett.*, vol. 20, no. 5, pp. 922–925, May 2016.

[34] F. Kulsoom, A. Vizziello, R. Borra, and P. Savazzi, "Reduced complexity Kalman filtering for phase recovery in XPIC systems," *Phys. Commun.*, vol. 29, pp. 112–119, Aug. 2018.

[35] W. Zongshuai and J. Zhu, "Baseband cross-poarization interference cancellation based on SCS algorithm," in *Proc. 12th IEEE Int. Conf. Electron. Meas. Instrum. (ICEMI)*, Qingdao, China, Jul. 2015, pp. 336–340.

[36] J. Yang, J. Chen, W. Wang, and L. Xu, "Joint XPI and ISI cancellation for dually-polarized radio systems over Earth-space links," *Procedia Eng.*, vol. 29, pp. 3217–3221, Dec. 2012.

[37] N. H. Noordin, A. O. El-Rayis, N. Haridas, B. Flynn, A. T. Erdogan, and T. Arslan, "Triangular lattices for mutual coupling reduction in patch antenna arrays," in *Proc. Loughborough Antennas Propag. Conf.*, Loughborough, U.K., Nov. 2011, pp. 1–4.

[38] Y.-S. Chen and H.-C. Zhou, "An isolation-enhanced quad-element antenna using suspended solid wires for LTE small-cell base stations," *Radio Sci.*, vol. 52, no. 5, pp. 663–676, May 2017.

[39] *5G Millimeter Wave Frequencies and Mobile Networks: A Technology Whitepaper on Key Features and Challenges*. Accessed: May 20, 2020. [Online]. Available: https://www.skyworksinc.com/-/media/SkyWorks/Documents/Articles/IWPC_062019.pdf

[40] Y. Huo, X. Dong, and W. Xu, "5G cellular user equipment: From theory to practical hardware design," *IEEE Access*, vol. 5, pp. 13992–14010, 2017.

[41] M.-J. Park, "Dual-band Wilkinson divider with coupled output port extensions," *IEEE Trans. Microw. Theory Techn.*, vol. 57, no. 9, pp. 2232–2237, Sep. 2009.

[42] Y. Wu, Y. Liu, and Q. Xue, "An analytical approach for a novel coupled-line dual-band Wilkinson power divider," *IEEE Trans. Microw. Theory Techn.*, vol. 59, no. 2, pp. 286–294, Feb. 2011.

HSIN-NAN HU was born in Taipei, Taiwan, in 1977. He received the B.S. degree in electronic engineering from the Ming Chi University of Technology, New Taipei City, Taiwan, in 2004, and the M.S. degree in electronic engineering from the National Taipei University of Technology, Taipei, in 2020.

Since 2005, he has been with the Foxconn Technology Group, as an Electronic Hardware Design Manager, where he is currently responsible for RF system integration design, which are including embedded antenna design, RF front-end hardware design, and RF system de-sense/coexistence issue debugging. His current research interests include millimeter-wave array antenna design, 5G RF font-end hardware design, and CATR test systems.

FEI-PENG LAI was born in Chiayi, Taiwan. She received the B.S. degree in electronic engineering from the National Taipei University of Technology, in 2017, where she is currently pursuing the Ph.D. degree in electronic engineering. Her current research interests include chipless RFID, antennas, and wireless communications. She has participated in numerous research projects, including 60-GHz on-chip antennas from KaiKuTek, Taiwan, and chipless RFID development from the Ministry of Science and Technology, Taiwan. She has served on the Reviewer Board for IEEE Access.

YEN-SHENG CHEN (Member, IEEE) was born in Taichung, Taiwan. He received the B.S. degree in electrical engineering and the M.S. and Ph.D. degrees in communication engineering from National Taiwan University, Taipei, Taiwan, in 2007, 2009, and 2012, respectively.

Since 2013, he has been a Faculty Member with the Department of Electronic Engineering, National Taipei University of Technology, Taipei, where he is currently a Professor. He has participated in a wide range of research projects, including chipless RF identification, mm-wave antennas and circuits, RF energy harvesting, antenna array failure correction, antennas for body centric communications, microwave reconfigurable components, and multi-objective optimization techniques. His recent researches focus include chipless sensor networks, high-gain antennas, and antenna theory.

Dr. Chen was a recipient of the Outstanding Reviewers Award from the IEEE Antennas and Wireless Propagation Letters, from 2017 to 2020, the Outstanding Reviewers Award from the IEEE Transactions on Antennas and Propagation, in 2019, the Outstanding Research Award from the College of Electrical Engineering and Computer Science, National Taipei University of Technology, in 2018 and 2019, respectively, the Outstanding Research Award from the National Taipei University of Technology, in 2019, and the Dr. Shechtman Young Researcher Award from the National Taipei University of Technology, in 2018. He has served on the editorial/review boards for many technical journals, transactions, proceedings, and letters.